Classification of UXO and non-UXO from magnetic anomaly data: a case study on inversion of drone magnetic data from Romo, Denmark

Wigh, Mark David; Kolster, Mick Emil; Hansen, Thomas Mejer; Dossing, Arne

Published in:
Geophysical Journal International

Link to article, DOI:
10.1093/gji/ggad097

Publication date:
2023

Document Version
Publisher's PDF, also known as Version of record

Geophysical Journal International

Geophys. J. Int. (2023) **234,** 915–932
Advance Access publication 2023 March 09
GJI Geophysical Journal International

https://doi.org/10.1093/gji/ggad097

Classification of UXO and non-UXO from magnetic anomaly data: a case study on inversion of drone magnetic data from Rømø, Denmark

Mark David Wigh [1], Mick Emil Kolster [1], Thomas Mejer Hansen [2] and Arne Døssing [1,3]

[1] *CMAGTRES, Crustal Magnetism Technology and Research Group, DTU Space, Technical University of Denmark, Centrifugevej* 356, *Denmark. E-mail: mdwi@space.dtu.dk*
[2] *Department of Geoscience, Aarhus University, Høgh guldbergs-gade* 2, *Denmark*
[3] *DTU CERE, Center for Energy Resources Engineering , Kolonnevej, Denmark*

Accepted 2023 March 3. Received 2023 February 28; in original form 2022 December 7

SUMMARY

A test site containing 24 targets of various disarmed unexploded ordnance (UXO) and non-UXO items were placed on a beach on the island of Rømø (Denmark) in a 600 m × 100 m area. Scalar magnetic anomalies were measured at 3–5 m altitude using an uncrewed aerial vehicle (UAV), towing a bird with a three-sensor triangular configuration to achieve a dense coverage with flight lines of 2 m spacing. The triple-sensor data set is utilized in a probabilistic inversion setup to infer the magnetic moments of the 24 targets. The purpose of the study, is to try and distinguish between different types of ferromagnetic objects (UXO, non-UXO) using magnetic anomaly data. The inversion methodology uses different forward models (prolate spheroids, rectangular prisms) to infer target shape, size and orientation in an attempt to discriminate between UXO and non-UXO items. Stochastic inversions are carried out using different prior assumptions of remanent magnetization strength (10, 50 and 80 per cent) of the induced dipole moment. Among the three levels of remanent magnetization strength in the prior, only some cases of discrimination seem evident for the lowest strength of remanence. One item is correctly classified as a true-negative (i.e. non-UXO) when assuming low remanent magnetization strength (10 per cent of the induced moment). However, at low remanent strength, one false-negative classification emerges, making any discrimination unreliable when assuming such low remanent magnetization. In addition to the discrimination study, different covariance models are utilized to optimize the inversion by addressing correlated errors and noise in the triple-sensor data set. Three covariance models are tested to try and account for spatially correlated noise and potential errors among the three sensors of each overflight. In many cases, the covariance models presented show a potential increase in sampling efficiency and consistency between data and the noise model, suggesting a more robust approach to a noise model in magnetic anomaly inversions. If the noise model is poor, however, it may bias the results by addressing the anomaly signal as noise. The inversions with correlated noise models are compared with inversions using a simple uncorrelated noise model. For several cases of data anomalies, differences between the inversion estimates when using correlated and uncorrelated noise models were evident, indicating that some bias may appear when assuming uncorrelated noise. Due to the general high presence of correlated signals in magnetic survey data, correlated noise models can significantly improve the overall uncertainty estimate of the estimated dipole moment. The study demonstrates, in terms of the 24 targets considered, that discrimination between UXO and non-UXO using magnetics is difficult. However, when using scalar magnetic data of high quality and resolution, the estimated dipole moments are often well resolved and uniquely defined in magnitude and position. This could provide valuable posterior information for future inversion studies by building a library of inferred magnetic moments from targets that have been found and inspected.

Key words: Inverse theory; Probability distributions; Magnetic anomalies: modelling and interpretation; Correlated noise; Covariance models.

1 INTRODUCTION

Unexploded ordnance (UXO) are continuously posing a threat in former war zones or military exercise fields, causing potential hazardous risks. UXO can be found in land areas and offshore environments, hindering effective use of locations in construction aspects and the inhabitation of post-war land.

UXO generally consist of ferromagnetic material that can be sensed remotely using geophysical methods such as magnetics or electromagnetic induction (EMI). They can be utilized alone or in combination to supplement combined knowledge from the data. In terms of efficiency, magnetic surveying is often significantly faster and easier to handle, while EMI can be ineffective for coverage of larger areas. In terms of characterizing the magnetic signature concerning source object shape/size, EMI has advantages because it is less affected by any remanent magnetization that might be present in the objects. However, due to the benefits of magnetic surveying, it is usually the only affordable method for large-scale data sets, so any possible target characterization from the magnetic signature would be highly valuable. In this study, magnetic survey data acquired from drone will be used to try and infer object shape and size by inversion and modelling of magnetic signatures from objects in the survey site. The survey data is from a survey campaign at Rømø, Denmark, where 24 objects were laid out in a closed area, and the magnetic anomalies were measured with a drone setup towing a triple-sensor bird equipped with three rubidium optically pumped sensors (Kolster *et al.* 2022). The 24 objects were a mixture of ferromagnetic objects and one ordnance of aluminium. Some were UXO, and others were non-UXO objects representing common objects in the nearshore/offshore environment.

Magnetic surveying is an effective geophyiscal method for UXO detection. Ferromagnetic objects have a magnetic signature due to the influence of the inducing geomagnetic field, resulting in magnetic anomalies seen in the magnetic surveys. These anomalies give the viewer information on where to find targets but do not provide any information on the type of target causing the anomaly. In this study, high-quality magnetic anomaly data will be used in the attempt to infer details on shallow magnetic sources and provide a robust approach for interpretation and modelling of magnetic anomalies. The aim is to discriminate between UXO and non-UXO objects by inferring target shape and size while accounting for remanent magnetization present in the sources. A probabilistic inversion approach (Wigh *et al.* 2020, 2021) will be applied to try to discriminate between UXO and non-UXO objects. Methods for optimizing the inversion of multiple sensor setups are also discussed.

Utilizing magnetic anomaly data to classify and discriminate between UXO and non-UXO sources have been researched for many years, where spheroidal approximations to the induced magnetization distribution of typical UXO have proven to be an effective application for modelling sources (Altshuler 1996; Butler *et al.* 1998; Billings 2004, 2006). However, remanent magnetization is well known to limit the viability of classifying ferromagnetic objects from the magnetic anomaly (Billings & Youmans 2006; Billings 2009; Wigh *et al.* 2020). A prerequisite for classifying magnetic sources from their respective anomalies is that the acquired magnetic data must qualify sufficiently well in spatial data sampling and accuracy. Recent advancements have been made in survey data quality and efficiency by using uncrewed aerial vehicles (UAVs) towing magnetometers (e.g. Walter *et al.* 2020; Døssing *et al.* 2021; Kolster & Døssing 2021a, b; Cunningham *et al.* 2021), making it possible to obtain a more precise estimate of the magnetic dipole moment. The work on UXO inversion using UAV magnetic survey data is limited in quantity, but progress has been made in recent years (Kolster & Døssing 2021a, b; Døssing *et al.* 2021; Kolster *et al.* 2022). In this study, the data used have previously been presented in Kolster *et al.* (2022), where a deterministic and a probabilistic approach have been used to estimate point dipole moments of different UXO in the survey data. In this study, the same data will be used to classify and discriminate between UXO and non-UXO.

In this study, a triple sensor setup of magnetometers are utilized in a point-down triangle configuration. The data acquired with the triple-sensor magnetometer bird setup is of high quality, both in terms of low instrumental noise and accurate sensor positioning, with sufficiently dense line spacing due to the coverage of multiple sensors and general high efficiency in surveying. While the main conclusion from Kolster *et al.* (2022) indicated that all three sensors were optimal to include as part of the inversion, results from using the single lower sensor often provided reasonable results in the estimated position and magnetic moment. In this study, we will primarily use the triple sensor data set, upon which several inversions with different noise models are carried out

Five individual inversion setups with different noise models are introduced for the purpose of classification and discrimination of UXO/non-UXO sources. This is done by inferring shape and size using two different forward models, from which a relative probability of UXO/non-UXO could be estimated using the posterior samples for each of the different inversion setups. The discrimination study aims at classifying the shape of the anomaly source using the two forward models of prolate spheroids and rectangular prisms, similar to what has previously been done for a synthetic study (Wigh *et al.* 2021). The discrimination study is carried out for three different prior assumptions of remanent magnetization strength in the sources, categorized with a remanent strength of 10, 50 and 80 per cent of the induced magnetization.

2 METHODOLOGY

2.1 Magnetic drone survey data from Rømø campaign

The 24 targets are pictured in Fig. 1, with additional information appended in Table 1. Each target was measured and weighted after the survey campaign. Additionally, a simple test was made using a small permanent magnet. If the magnet did not stick to a specific part of the object, it was classified as a non-ferromagnetic part. Weaker magnetic contributions (such as ferrimagnetic material which cannot be completely discarded, but is assumed to have no significant contribution.)

Preprocessing and handling of the triple-sensor bird data is presented in Kolster *et al.* (2022). Only minor preprocessing of the data has been carried out (small wavelength components have been removed using FFT component analysis). In addition to this, the along track difference (ATD) is used as a tool for highlighting short wavelength signals (such as signals from UXO) in the data. The

Figure 1. Items positioned in the survey area. Pictures originally from Kolster *et al.* (2022).

ATD is set to calculate the difference between every 8th-datapoint (which is done for all datapoints in the flight line). The distance between every 8th datapoint can be assumed constant for all practical purposes but may have minor fluctuations if the drone adjusts the flight velocity or path in a survey line.

2.2 Probabilistic inversion setup

A general formulation of the inverse problem involves determining some model parameters, **m**, that are related to some data, **d**, through the forward function, g:

$$\mathbf{d} = g(\mathbf{m}) \tag{1}$$

The inverse problem is the study of determining the model parameters from the measured data, which often are indirect measurements of the model we want to estimate. This is generally not a simple case. when the data are contaminated by unwanted signals and errors or the forward relation might be imperfect.

Inversion of the magnetic data is carried out using a probabilistic setup, where the posterior distribution is sampled in a stochastic inversion process. The posterior distribution describes the combined

Table 1. Overview table for the UXO, UXO fragments and debris objects placed inside the survey area. Table originally from Kolster *et al.* (2022).

No.	Weight	Description	Notes
1	11.8 kg	Small airdropped	L64 cm, Ø5.7 to 9 cm
2–6	26.2 ± 1.4 kg	155mm shell	L57 cm; Ø5.5 to 16 cm
7	34.3 kg	Cannonball (half)	Ø33 cm. From 'Slaget på Reden'
8	14.5 kg	Hinged L-beam	L93 cm, H13 cm
9	7.4 kg	Metal disc	H10 cm, Ø36 cm
10	26.2 ± 1.4 kg	155mm shell	L57 cm, 5.5 to 16 cm
11	12.3 kg	Partial metal plate	L50 cm, 43 cm, and 23 cm. H1 cm
12	19.7 kg	Square metal plate	L50 cm, H1 cm
13	?	Unknown object	L93 cm, Ø5 to 14 cm. Only tail magnetic
14	8.1 kg	Training Rocket	L95 cm, Ø7 cm. Only tip magnetic.
15	9.0 kg	Bent tail fin	L65 cm, Ø23 cm
16	6.0 kg	Airdropped	L120 cm, Ø20 cm
17	17.1 kg	Fire extinguisher	L83 cm, Ø14 cm
18	14.9 kg	Round black sphere	H42 cm, Ø45 cm
19	14.5 kg	Bouyant sea mine "316"	L60 cm, Ø25 cm
20	20.3 kg	Alu. seamine fragment	H40 cm, Ø65 cm
21	47.9 kg	Depth charge	L70 cm, Ø43 cm
22	26.3 kg	Bouyant sea mine "315"	L79 cm, Ø32 cm
23	48.3 kg	5-In training rocket	L204 cm, Ø13 cm.
24	34.4 kg	Aluminium winch	L130 cm, Ø40 cm

information from prior knowledge with new information that may be acquired from the data. The probabilistic inversion setup requires one to be able to evaluate the model response with respect to the data, which can be done as long as a forward model and data noise model are defined. From the definition in Tarantola (2005), the posterior probability density (PD), $\sigma_m(\mathbf{m})$, over the model parameters can be expressed by

$$\sigma_m(\mathbf{m}) = kL(\mathbf{m})\rho_m(\mathbf{m}), \tag{2}$$

where $L(\mathbf{m})$ is the likelihood function giving an estimate of fit between the model and data, and $\rho(\mathbf{m})$ is the prior model PD. The likelihood function is described by :

$$L(\mathbf{m}) = \int_D d\mathbf{d}\frac{\rho_D(\mathbf{d})\theta(\mathbf{d}|\mathbf{m})}{\mu_D(\mathbf{d})}, \tag{3}$$

where $\rho_D(\mathbf{d})$ is describing the measurement uncertainties (e.g. errors caused by uncertainties in the instruments or unwanted signals contaminated in the data). $\theta(\mathbf{d}|\mathbf{m})$ is the theoretical probability density representing errors related to solving the forward problem and $\mu_M(\mathbf{m})$ is the homogeneous probability density, ensuring the parametrization is invariant to changes in the coordinate system. Under the condition of a linear dataspace (e.g. Cartesian), and an assumption of zero theoretical error in the forward relation between data and model prediction [perfect relation in $d = g(m)$], then the likelihood is determined by the measurement uncertainties of the data:

$$L(\mathbf{m}) = \rho_D(g(m)). \tag{4}$$

In general, unless dealing with linear inverse Gaussian problems, it is not possible to analytically describe the posterior distribution. Instead, sampling methods can be used that will generate a sample of the posterior distributions, from which, and if the sample is large enough, any statistics of the posterior distribution, can be obtained, see for example Mosegaard & Sambrigde (2002). Here we use a combination of the extended Metropolis algorithm (Mosegaard & Tarantola 1995) and Gibbs sampling (Geman & Geman 1984) to sample the posterior distribution, eq. (2), referred to as Gibbs-within-Metropolis. The algorithm is utilized in the Matlab software package, SIPPI (Hansen *et al.* 2013a), and has previously been used in magnetic UXO modelling and inversion. Further details on the inversion setup will be omitted here but can be found in details in Wigh *et al.* (2020, 2021)

2.2.1 *Classification of targets*

The classification of targets is done by assigning a relative probability to each of the classes/hypotheses by using the average posterior likelihood from the posterior distributions. If one has two hypotheses (such as 2 different priors or forward models) the relative probability of each hypothesis, $\mathcal{H}$, can be computed from the average posterior likelihood. If $\mathbf{M}^*_\sigma = [\mathbf{m}_{\sigma}{}^*_1, ..., \mathbf{m}_{\sigma}{}^*_{N_r}]$ is a sample of N_r realizations of $\sigma(\mathbf{m}|\mathbf{d}_{\text{obs}}, \mathcal{H}_i)$, then the average posterior likelihood $L_{P-\text{Avg}}$ can be computed for each hypothesis as

$$L_{P-\text{Avg}}(\mathcal{H}_i) = \frac{1}{N_r}\sum_i^{N_r} L(\mathbf{m}_{\sigma i}{}^*|\mathbf{d}_{\text{obs}}, \mathcal{H}_i). \tag{5}$$

Eq. (5) will be used to compare the three different class inversions by determining the relative probability using the average posterior likelihood estimates. However, it can not be used to compare the posterior distributions that have been sampled under different noise assumptions. It has previously been referred to as posterior evidence (Wigh *et al.* 2021), due to the fact that the posterior likelihood is an average likelihood from a sample of the posterior, whereas the general evidence is defined as the average likelihood of a sample from the prior.

2.3 Inversion of shape and size: forward models

The spheroid and prism forward models used for classification generate a similar point-dipole moment. The induced dipole moment may be reproducible by both forward models, but in some cases, the two forward models are uniquely defined. This is due to the prior constraints on aspect ratio and orientation since an induced dipole moment is inferred from an assumed shape with a specific aspect ratio, orientation and volume. With the inclusion of remanent magnetization, the number of model parameters is further increased as well as the non-uniqueness between the forward models. The spheroid model has been used extensively to model various UXO with similar shapes (Altshuler 1996; Butler *et al.* 1998; Billings 2006). The demagnetization factors for a spheroid can be analytically determined and used to produce the induced dipole moment.

Approximations to non-UXO objects are made by utilizing rectangular prisms to simulate non-UXO shapes (long rods and flat plates) that are expected to be found in similar environments as UXO. The prism forward model approximates demagnetization factors from the two aspect ratios defining the shape of the prism. Further details on the forward models can be found in Wigh *et al.* (2021). The prior models and related parameters assigned for each of the forwards are shown in Table 2. The prism forward is used with two different priors, one represents a flat plate item and the second represents elongated rod objects. The last class is the spheroid class which represents possible UXO targets. Another forward model is the simple point-dipole moment, where the dipole-fit is sampled

Table 2. Prior models used in the simple dipole moment inversion and the three conceptual models of spheroids (UXO), rods and plates. The first group of parameters are globally shared that have equal range for each conceptual model, while the second to fourth groups define the unique priors. All prior models are represented by uniform distributions (Uni. dist) with a chosen range.

Shared global priors	Range (min,max) Uni. Dist.
Depth (*z*-position relative to expected surface height)	–0.6 to 7.5 [m]
Phi angle	[–90, 90]
Theta angle	[-35, 35]
x-position	±4 m
y- position	±4 m
Inclination *Mrem*	[–90, 90]
Declination *Mrem*	[0, 360]
Prism prior	range (min,max) Uni. Dist.
λ_y	Rod; [0.05, 0.008] Plate; [1.2, 0.82]
λ_z	Rod; [0.005, 0.0008] Plate ;[0.3, 0.004]
Gamma angle	Rod ;[–90, 90]; Plate [–35,35]
Kg steel	30–400 [kg]
Mrem strength	[10, 50, 80] % of induced moment
Prolate spheroid prior	range (min,max) Uni. Dist.
Aspect ratio, *e* (Spheroid)	1.1–7
Kg steel	30–400 [kg]
Mrem strength	[10, 50, 80] % of induced moment
Dipole moment prior	range (min,max) Uni. Dist.
m_x, m_y, m_z	0–8 [Am^2]

independently of shape, size or orientation, in which case it is class-independent. It is used to quality check the other forward and prior models (both in terms of convergence and the selection of remanent magnetization strength).

2.4 Noise models

In an ideal setup, the noise model describes a realistic distribution of expected data errors and uncertainties. Setting up a noise model, in practice, is easy if the errors and noise signals are uncorrelated and normally distributed but become increasingly complex when correlated noise and errors need to be accounted for. In magnetic surveying, the measured signal will be a superposition of all magnetic fields at the observer point, making each data point heavily correlated with adjacent points (if there are nearby magnetic contributions from other objects not considered in the inversion or a strong background field, for example). Hence, if there are magnetic contributions originating from sources other than the object of interest, then that signal will interfere as a residual field with high spatial correlation, which may affect the model estimate provided that the noise model is assumed Gaussian uncorrelated.

Some examples of what could contribute as correlated data noise in the anomaly data include near surface geology, contributions from ferromagnetic (human-made) sources not considered in the inversion, Noise from the drone (instruments, engines), data errors (positional uncertainties/errors of the sensor, sensor biases) and measurement errors. Some of these uncertainties might affect all of the sensors at different strengths of correlation due to the setup of the triple-sensor bird. For instance, a height error in the bird for a single survey line will have an effect on all of the three sensors.

Table 3. The five different inversion setups utilized in the study. Four of these use the same data input (triple-sensor data set), while one only utilizes data from the single lower sensor. Three out of the five setups utilize covariance models (generated using a spherical variogram with specified variance and anisotropic correlation length). The estimated variance in the noise model for the first inversion setup is calculated from a signal-to-noise ratio (SNR) for each anomaly. The four last setups utilize a fixed variance denoted by a standard deviation (STD) and the associated variance (var)

Inversion setup (data + noise model)	Variance
(1) Single-(lower) sensor uncorrelated noise (fixed SNR)	SNR = 3
(2) Triple-sensor uncorrelated noise (fixed STD)	std = 0.0328 nT
(3) Triple-sensor correlated noise (line-correlation)	std = 0.0332 nT, var = 0.0011
(4) Triple-sensor correlated noise (spatial-correlation)	std = 0.0158 nT, var = 2.5e-4, range (2 m + 8 m)
(5) Triple-sensor correlated noise (line- + spatial-correlation)	std = 0.0141 nT, var = 2.0e-4, range (8 m)

Therefore, we propose to describe these types of correlated noise by the following correlated Gaussian models:

$\mathbf{C}_{d\,\mathrm{line}}$ (Line-correlation): Assumed correlated noise along each line (between all three sensors in the magnetometer bird) for every overpass (i.e. for one fly-over the noise on all three sensors is assumed to be correlated).

$\mathbf{C}_{d\,\mathrm{space}}$(Spatial-correlation): A noise model that introduces correlations among nearby and adjacent data points. A geostatistical variogram model was used to simulate spatial correlations, previously used in hydrogeophysics to account for subsurface variations (Hansen *et al.* 2008, 2013b). The structure is chosen as spherical and does require a length input to define the length of correlated 2-D structures. The structures generated with appropriate ranges seem to have similarities to the background variations that are apparent in the survey. It can also be used to account for local data errors/noise/modelling errors.

By combining the two covariance matrices through addition (e.g. Mosegaard & Tarantola 2002) the data covariance matrix is obtained:

$$\mathbf{C}_d = \mathbf{C}_{d\,\mathrm{line}} + \mathbf{C}_{d\,\mathrm{space}}. \tag{6}$$

In total, three different covariance models will be tested on the triple-sensor data set: (1) Covariance matrix with line correlations between line groups of the three sensors (2) Covariance matrix with spatial correlation. (3) Combination of (1) and (2).

If the measurement uncertainty can be described by a Gaussian correlated model with mean $\mathbf{d}_d$ and covariance $\mathbf{C}_d$, the likelihood function can be expressed as (see e.g. Hansen *et al.* 2014)

$$L(\mathbf{m}) = k\ \exp\left(-\frac{1}{2}(g(\mathbf{m}) - \mathbf{d}_{\mathrm{obs}} - \mathbf{d}_d)^T \mathbf{C}_d^{-1}(g(\mathbf{m}) - \mathbf{d}_{\mathrm{obs}} - \mathbf{d}_d)\right). \tag{7}$$

To assess the different covariance models applied, multiple inversions have been carried out with varying models of noise assigned to the data structure for each inversion setup, as presented in the bottom section of Table 3. The first and most straightforward setup of the noise models is by assuming uncorrelated Gaussian noise, which is done once using the lower single-sensor data (assuming a fixed SNR) and once using the triple-sensor data set (assuming a fixed STD). The last three inversion setups utilize data from the three sensors with the addition of a data covariance matrix.

Difficulties that arise when inferring more complex model spaces, such as the spheroid and prism forward models, are expected to be reduced by applying models for correlated data errors to the triple-sensor data set, supposing it imitates some of the correlated errors in the real data. This should mitigate sampling issues while providing a more realistic noise model that might represent the data noise better (i.e. correlated signals will often be present in a geospatial magnetic survey).

Since modelling of a covariance matrix significantly increases the inversion complexity, it might result in a significant loss of efficiency when an abundant amount of data is included. Tests have been carried out using a 4× downsampled version of the triple-sensor data (sampled at 200Hz) set without losing spatial resolution or performance in the model prediction (except for a possible reduction in performance for the smallest targets). This helps sampling and increases the efficiency significantly since we reduce the size of the data covariance matrix by 75 per cent (e.g. a C_d matrix is reduced to 2500×2500 instead of $10\,000 \times 10\,000$ due to the high sampling rate of the sensors). Effects of the downsampling would appear as a reduction in the positional accuracy of the target during inversion, with a primary reduction in the estimate of source depth (whereas a reduction in line spacing density would affect the horizontal positioning of the source). The depth and horizontal prediction of the targets from inversions are sufficient in accuracy and usually well resolved (with a slight decrease in accuracy and precision when the correlated noise models are utilized).

3 RESULTS

The first part of the results focuses on discrimination between spheroid and prism objects. For the inversion analysis, the dataset used will contain data from all three sensors, except for one case where only the lowest sensor is used. The use of the lower sensor has previously shown promising results (Kolster *et al.* 2022) to achieve a reliable estimate of the magnetic moment (at least for the larger objects). One inversion scheme is established using the single lower sensor with uncorrelated noise, while the remaining setups focus on inversion of the data containing all three sensors. For the triple-sensor case, inversions have been done with and without correlated noise to test and quantify the sampling efficiency and assess differences in the estimated magnetic moments. All inversion setups are carried out for different assumptions of remanent magnetization, ranging from 0 to 10 per cent, 0–50 per cent and 0–80 per cent relative to the induced magnetization.

3.1 Inversion and classification of target sources

The different covariance matrices that have been used, are denoted as line, space and line + space covariance matrices. The three versions differ by one being a combination of line correlation and spatial correlation, for example $\mathbf{C}_d = \mathbf{C}_{d\,\mathrm{line}} + \mathbf{C}_{d\,\mathrm{space}}$, while the other two are generated with one of the two choices. The difference between the versions can be found in the spatial covariance matrix, where the first edition has a correlation range of 15 m and the second composes a combination of correlation lengths of 15 and 2 m with a slightly higher variance. In Fig. 2, an example of a covariance matrix (Line + space) and a realization of noise from this covariance matrix are illustrated.

Inversions of the 24 targets are carried out for three different assumptions of remanent magnetization. For the single sensor setup, only uncorrelated Gaussian noise models are used. In the first case, the spheroid and prism priors have 10 per cent remanent magnetization allowed as the maximum range, while for the second case, the remanent magnetization of the spheroid prior is increased to 50 per cent and, lastly, in the third, the maximum remanent magnetization is set to 80 per cent. Having sampled the posterior distribution for each forward model considered, the relative probability of each forward model is estimated by calculating the average posterior likelihood over the last 10k samples. The area plot of the probability computed from the average likelihoods is shown in Fig. 3. It is limited to showcase only with remanence assumed to be within 10 per cent. In fact, this is the only case of interest since the other two cases with higher remanence provide zero discriminatory capabilities.

The first column of Fig. 3 shows the relative probabilities when considering the spheroid and prism (rod + plate) forwards. In the second column, the simple dipole model is included in the assessment, serving as an independent quality check of the other inversions that infer target shape and size. The dipole moment model is independent of any assumptions on remanence and induced moment. Hence, if a reasonable fit is only achieved with the dipole model, then one of three scenarios could be the cause: (1) The remanent magnetization allowed in the prior is lower than the amount present in the source. (2) The target magnetic signature cannot be fully modelled by a spheroid/prism. (3) Convergence issues of spheroid/prism sampling. The run carried out with uncorrelated noise (Fig. 3a) exhibits potential convergence issues when comparing to the other inversions using correlated noise models, as can be seen with targets 1, 4, 8, 20 and 21 where only one of the shape inversion seems to converge properly.

A bottom bar plot (Fig. 3i) shows the mean estimated relative probabilities computed from the values above for the three classes. From the bar plot, two targets show discriminatory capabilities (Target 3 and 12). If the Line covariance inversion is left out (due to the perhaps unrealistically high noise), Target 23 also appears as an item that cannot be fitted equally by the shape models. It suggests target 23 to be a prism object (primarily a rod), which seems reasonable considering that it is a long cylindrical object with an aspect ratio (the long axis) of approximately 15, which is much higher than the spheroid prior allows. For target 12, some discrimination seems possible, but it has more of a plate shape than an elongated rod shape, yet the rod fits better, which could be due to remanent magnetization. Target 3 is a 155 mm grenade projectile and can only be fit by the rod prior, suggesting that the item has a significant remanent magnetization (i.e. >10 per cent) that results in a wrong classification.

An example of sampling using the different noise and forward models is showcased in Fig. 4. The figure shows the Log$L$ during sampling with all four conceptual models (spheroid, prisms) using the four noise models. An example of inversion of target 21 with 10 per cent remanent magnetization is shown. It is evident from the figure, that sampling with uncorrelated noise does not manage to converge in all cases. Additionally, the covariance noise models increase the obtained Log$L$ values closer to the range of $-N/2$ (where N is 1866 datapoints), suggesting a higher consistency between data and noise model.

3.1.1 Detailed inversion example of target 21 (80 per cent rem)

An example with inversion of the triple-sensor data set for target 21 (with 80 per cent) is shown in Figs 5 and 6. First, the dipole moment inversion with uncorrelated noise is presented, showcasing the data,

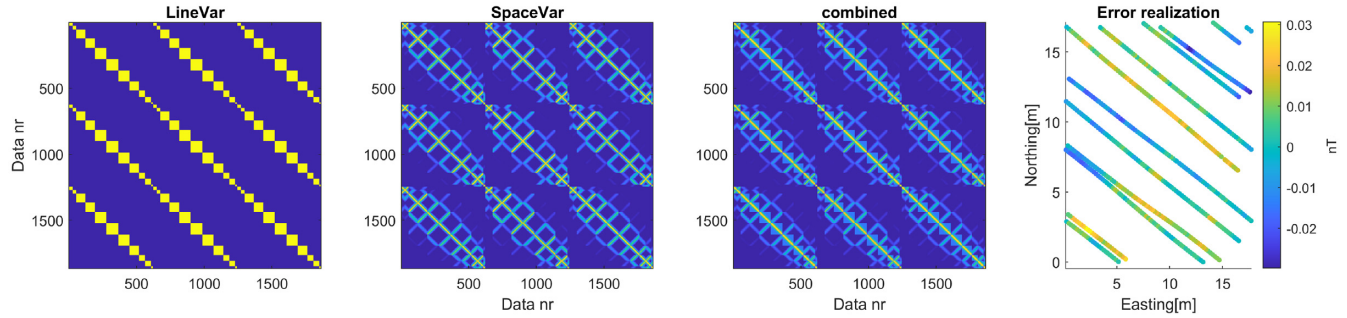

Figure 2. Example of data covariance matrix used for inversion of triple-sensor setup. The example shown is for target 21 using all three sensor data sets (downsampled 4×). The error realization is shown for the data points of the lower sensor only. The covariance matrix is made such that the variance of each data point is significantly lower than the case with uncorrelated Gaussian noise.

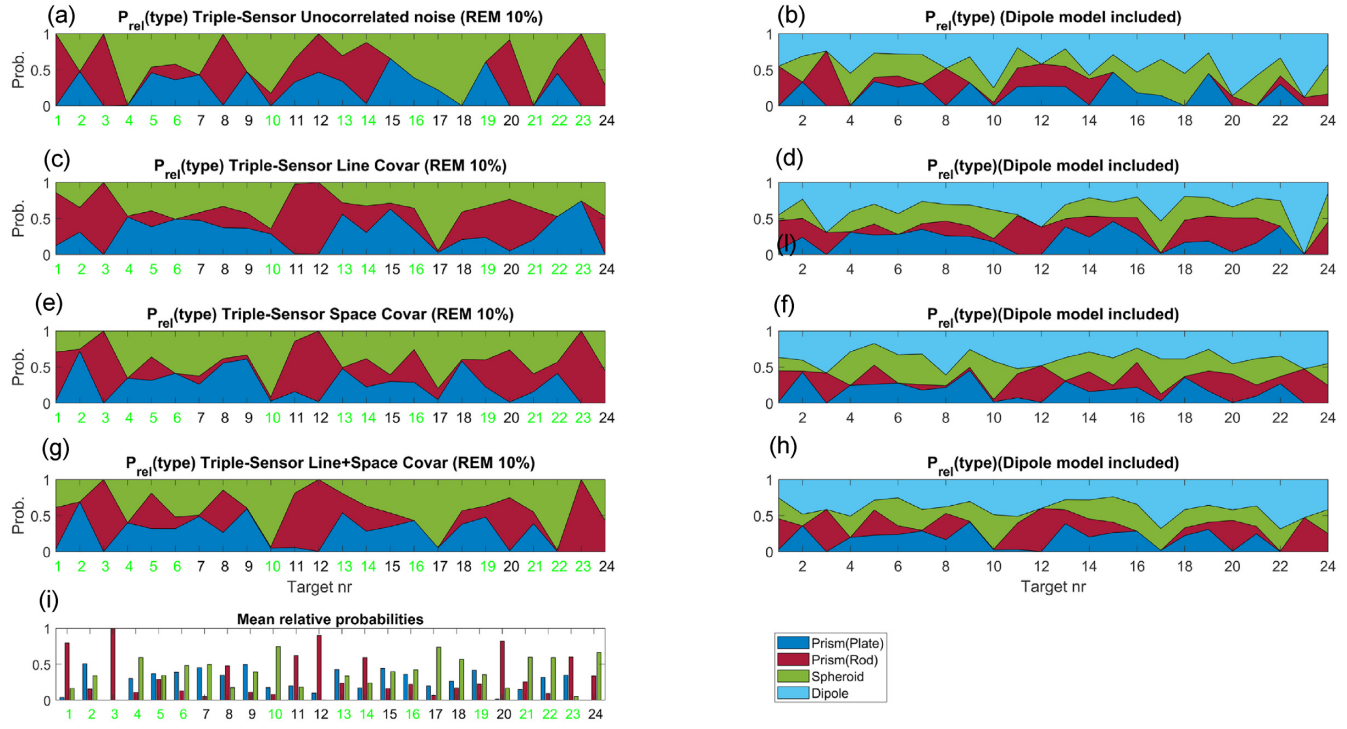

Figure 3. Comparison of the achieved models for the different forward and priors considered. For each row, the relative probabilities of each class are shown for the different noise models used. The first column shows the area-plot for the spheroid (green), prism rod (red) and prism plate (blue) forward models. In the second column, the simple dipole model (cyanic) inversion is included in the assessment, increasing the number of models used for comparison to four. A bar plot is seen in the last row (i), showing the mean class probabilities when averaging over the relative probabilities of each inversion setup. The triple sensor data set with different noise models and a fixed remanence of maximum 10 per cent have been used.

prediction and residual field for all three sensors (Fig. 5). Secondly, residual fields of the lower sensor from the four different inversion setups are presented in Fig. 6 to illustrate the estimated model variations due to the different correlated noise setups. It can be seen, that there is one line with a strong and highly correlated residual signal. This could be explained by a data error (e.g. sensor altitude positioning) or higher order moments in the source affecting the lower sensor. From inspection of the individual flight line altitudes (figure omitted here), the three middle lines above the target have an approximate altitude to the centre of target 21 at 5–5.2 m (distance from the lower sensor to the centre of the target). The survey lines in the outer regions vary slightly more between 4.2 and 5.6 m altitude. The flight lines with the lowest altitude, however, are farther away from the source than the centre lines, so higher order moments are unlikely to have any effect.

3.2 Overview plots of inversion results

To summarize on all of the different dipole moments obtained with the various inversion setups, Figs 7, 8, 9 and 10 are made for a presentable overview. The main figures (Figs 7, 8 and 9) present the magnetic moments for each assumption of remanence, acquired by inversion with the various inversion setups. The last figure (Fig. 10) presents the relative probability of all UXO inversions obtained. Since the magnetic dipole moment is the essential parameter for any classification, some figures will be highlighted and presented for better visualization due to the large amount of results.

Moments derived with the simple dipole model are presented in Fig. 7 (here remanence and shape/size inversion are avoided, that is it shows only model variability due to the different noise models). The magnetic moments derived with the spheroid and prism forward model with a prior assumption of 10 and 80 per cent remanent

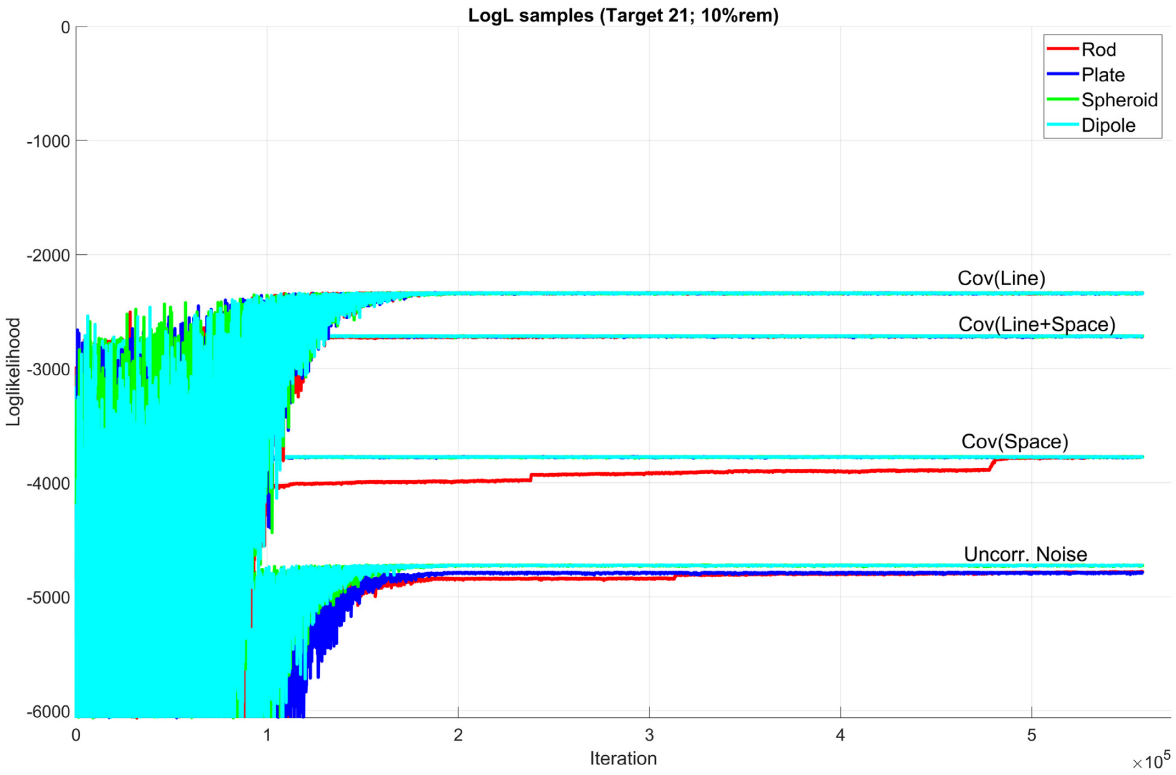

Figure 4. Log*L* samples of target 21 with 10 per cent remanence. Some sampling difficulties may appear for the uncorrelated noise model, especially when sampling with low remanence as is showcased here. For each noise model used (as denoted by the text above the Log*L* samples), four inversions are carried out using the different forward models [i.e. Red: Prism(Rod), blue: Prism(Plate), Green: Spheroid, cyanic: dipole moment sampling with no shape inference]. Number of data points in this example is $N = 1866$ (using data from all three sensors downsampled at 25 per cent).

magnetization are shown in Figs 8 and 9, respectively. The case with remanence of 50 per cent is excluded due to the high similarity with the former containing 80 per cent. The 10 per cent remanent case is the only case where certain discrimination is apparent among the different inversions (target 3, 12 and 23 which are highlighted at the bottom of Fig. 8), while the inversions with higher assumptions of remanence do not obtain any likely discrimination. Yet, the magnetic moments in the case with high remanence do indeed differ among the four forward models and the different inversion setups, reflecting some of the variability in magnetic moments due to the selected noise models (similar to the variations seen in Fig. 7 with moments derived using the simple dipole inversion).

The variations in estimated dipole moments for each target can be seen in Fig. 7, with some targets having a higher variation than others. The results achieved by inversion of the single sensor and triple sensor data with uncorrelated noise are in many cases similar, while the three inversion-setups using correlated noise models tend to vary more for each target estimate, especially for the larger magnetic anomalies (targets 21, 23 and 24) and also some smaller anomalies (targets 7, 14 and 15). This variation is due to the covariance models introduced, accounting for some of the spatial correlations in the survey data. However, care must be taken when using a correlated noise model since it can severely bias the results if the anomaly signal becomes part of the correlated noise model. Several tests were carried out with different covariance matrices of different spatial ranges and amplitude of the diagonal variance (e.g. STD of data points), from which it was clear, that the selected variance in the correlated noise models is very sensitive and should be significantly lower than the variance in the uncorrelated noise models (for this specific data set at least). This is mostly in terms of the space covariance matrix, where a high variance could give a significantly worse fit that does clearly not fit the magnetic anomaly sufficiently. However, the correlated noise models where only the line-covariance matrix is applied were not as sensitive to the chosen diagonal variance, and did fit the anomaly reasonably even with very high diagonal variances (e.g. the line correlation does not describe correlations similar to anomaly signals, which the space covariance is more likely to do).

In Fig. 8 the magnetic moments obtained with 10 per cent remanence are presented. The inversions are carried out with the three forwards (spheroid, rectangular prisms (with 2 different priors) and dipole moment) with the five different inversion setups (lower sensor, triple sensor, triple sensor with x3 correlated noise). As such, there are 20 estimates of the magnetic moment for each target, which have been plotted for visualization. The three targets where discrimination might be possible have been highlighted in a zoomed in view for improved visualization between the estimated moments of the three targets (bottom plot in Fig. 8). Here, it is apparent, how the simple dipole and rod prior inversions obtain a dipole moment different from the other shape inversions (mostly apparent in the *Z*-component), which elucidates the discriminatory capabilities seen. Besides this, some variation between the moments derived with each noise model is apparent and seems to have similar structures as the case with dipole moment sampling (Fig. 7), indicating that these variations are mainly due to the covariance noise models (and some inversions may not have been able to reproduce the anomaly properly due to the low remanence).

The magnetic moments achieved estimated with 80 per cent remanence in the prior is displayed in Fig. 9. Due to the high remanence allowed in the prior, all shape inversions are expected to

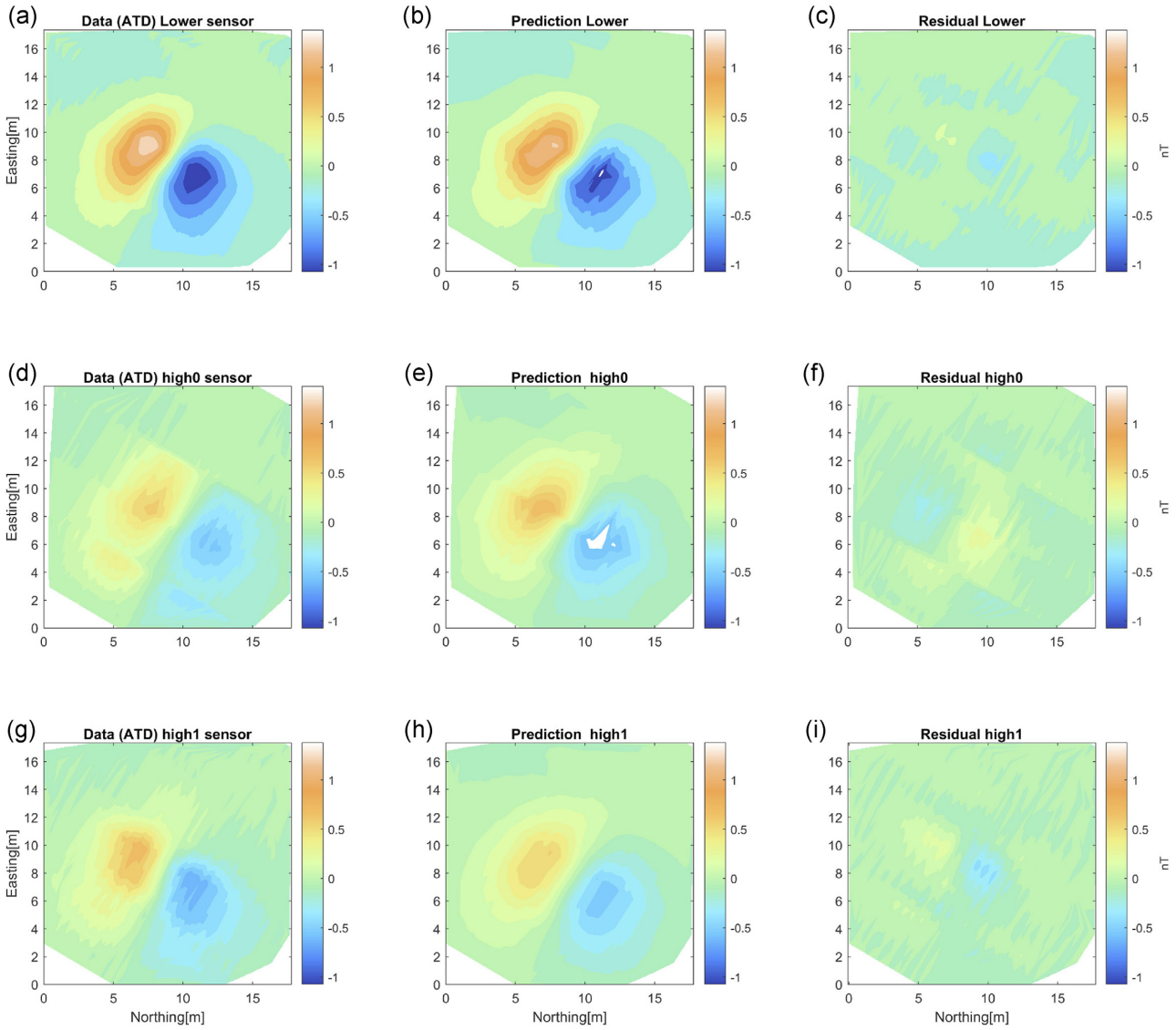

Figure 5. Example of fitting the data anomaly for target 21, shown for all three sensor data sets. The data are shown on the left, with the model prediction in the middle and the residual (data - model prediction) on the right plot. The model prediction is from sampling of the dipole model with uncorrelated noise (last sampled model in the posterior). (a–c) Lower sensor, (d–f): top left sensor and (g–i): top right sensor.

have converged to the same region as the inversions with the dipole moment. Hence, similar results are seen in Figs 9 and 7. For the targets with small magnetic moments (and hence anomaly amplitude), some variations are seen between the different shape inversions. This might be due to the covariance models not being scaled with anomaly amplitude causing a relatively higher effect since more of the anomaly signal might be considered noise. This appears to have a higher variation for the inversion with line covariance (which is also scaled with a high variance)

The bar-plot in Fig. 10 summarizes the chances of discriminating between UXO/non-UXO for the different inversions. The probability of being in the spheroid class (i.e. UXO, P_{UXO}) is shown for each target, for each of the five inversion setups. The only case where some discrimination between spheroid and prisms can be made is at a prior remanence of maximum 10 per cent. Here, target 12 is correctly classified as a prism, however, target 3 is also classified as a prism but is an UXO (155 mm grenade). Target 3 most likely contains more than 10 per cent of remanent strength which could explain why it becomes wrongly classified. Hence, certain risks of falsely discriminating are likely when the remanence is low, and the discrimination diminishes if the remanence is increased, which doesn't seem to allow for any discrimination possible without further assumptions on the remanent magnetization.

Variations in the P_{UXO} values appear for most targets, however, the values are generally quite consistent. This is mostly true for the three inversions carried out using the covariance models, whereas the inversions using lower sensor and triple sensor data with uncorrelated noise seem to have some outliers from the others with $P_{\mathrm{UXO}} = 0$ and $P_{\mathrm{UXO}} = 1$ (e.g. targets 4, 18, 21 and 24), which could be explained by convergence issues. However, when the five different inversion setups achieve similar relative probabilities the estimate is expected to be more robust, as is the case for targets 3 and 12 where $P_{\mathrm{UXO}} = 0$ at 10 per cent remanence. For target 23, we see that four out of the five inversion estimates suggest a non-UXO (rod object), indicating that some discriminatory capabilities are possible (target 23 is actually an UXO, but has an aspect ratio of approximately 15,

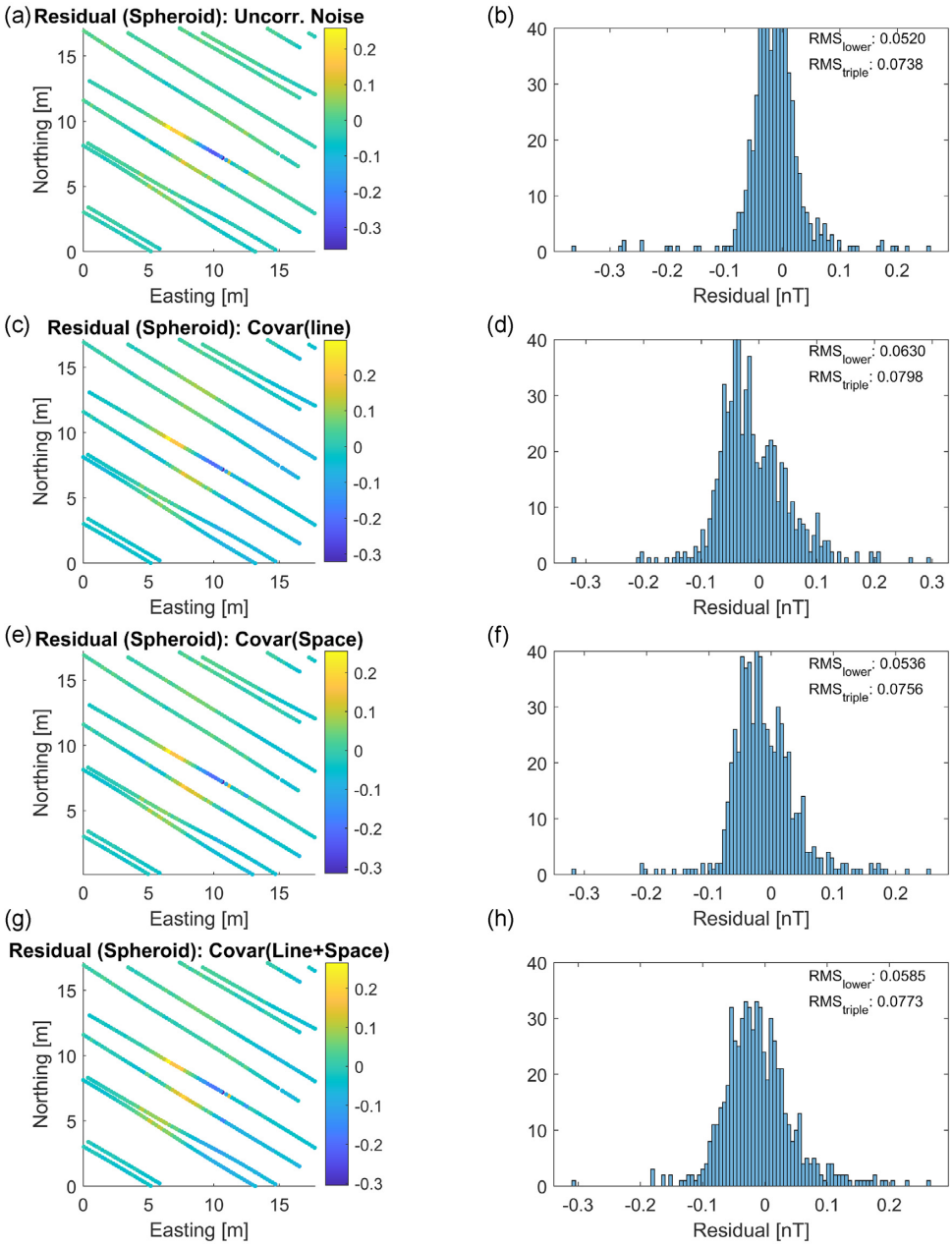

Figure 6. Scatterplot of the lower sensor residual (model-prediction) of target 21 for the four inversion setups. The model predictions are from sampling of the spheroid model with 80 per cent remanence (the last sampled model in the posterior). Histograms of the lower sensor residuals are shown accompanied by the root-mean-square residual value. (a–b): Inversion with lower sensor data set with uncorrelated noise, (c–d): Inversion with triple sensor data set, line-covariance noise model, (e–f): Inversion with the triple sensor data set, space-covariance noise model, (g–h): Inversion with the triple sensor data set, space- and line-covariance noise model.

which is much higher than the aspect ratio allowed in the spheroid prior).

The influence of discriminatory capabilities due to remanence is apparent in Fig. 10. Here, it is apparent how no discrimination can be done when a remanent magnetization of 50 or 80 per cent is allowed in the prior. If the remanent magnetization is constrained to a maximum of 10 per cent, we see that some targets are correctly estimated to be non-UXO items. However, some targets are incorrectly classified, posing major risks if it were to be used as a single tool for classification in real scenarios.

In Fig. 11, the estimated mean dipole moment have been plotted with targets sorted into their weight on the x-axis. The figure attempts at combining all information gathered from the different inversion setups. This has been done by taking the average of all the model estimates from the different inversion setups (i.e. the results shown in Fig. 7). In an attempt to quantify the uncertainty of this single estimate, the error bars are computed by taking the average of the individual STDs from the mean over the posterior samples, and the STD over the 5 different mean posterior models. By utilizing this as an error, it is evident that some targets are better resolved than others, where it must be assumed that noise and errors play a certain role here. It is evident from inspection of Fig. 11, that there is no simple correlation between target magnetic moment and target size. Remanent magnetization plays a major role here among other

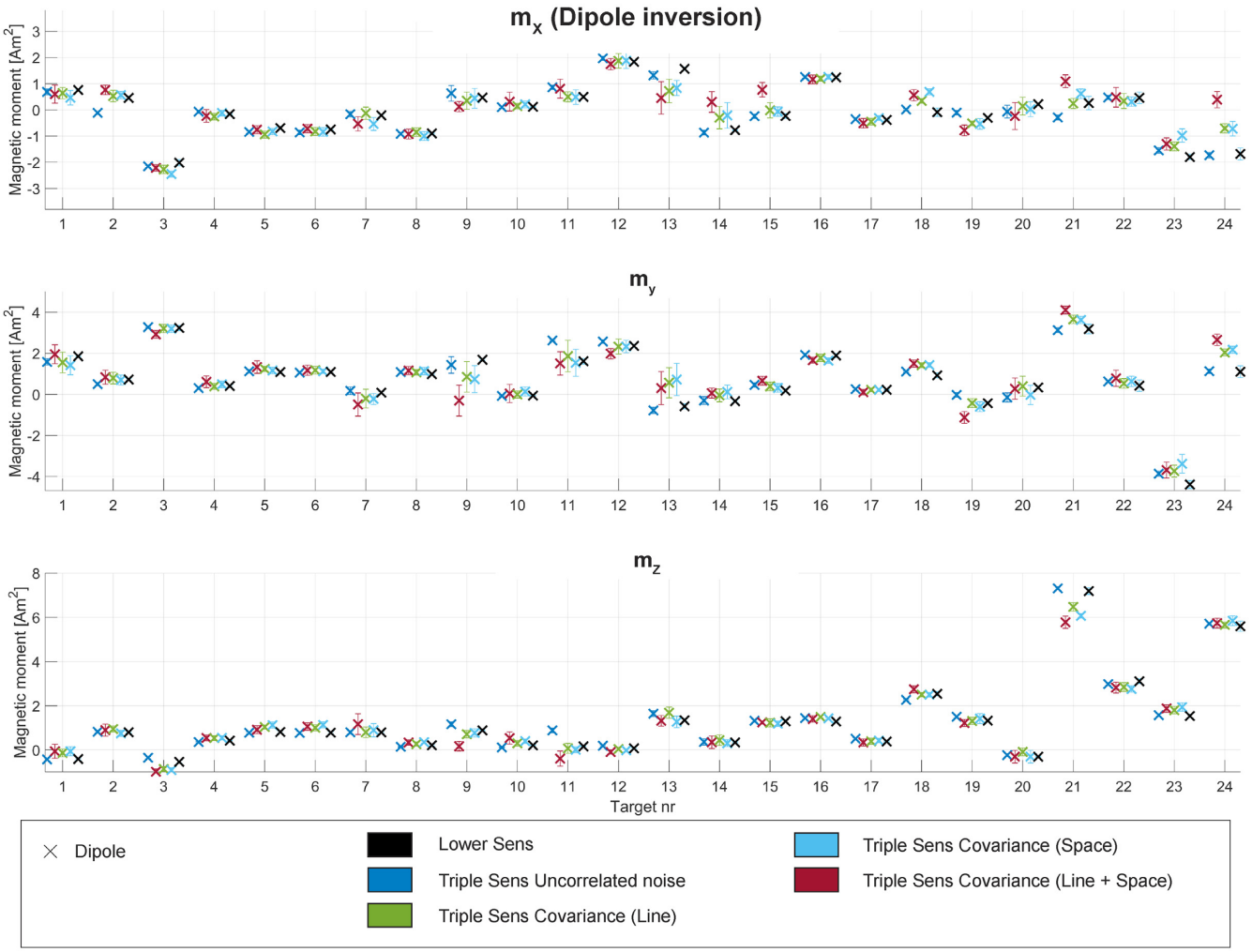

Figure 7. Mean estimated dipole moments from inversions using the different noise models. All estimates shown here are achieved using the simple dipole moment inversion (no inference of shape/size), by taking a mean of the last 5 posterior samples (and error bars showing the standard deviation of the last 10 samples). The figure gives an illustration of the variability due to the different noise models utilized in the inversions.

factors related to the induced moment such as the orientation and shape of the target.

3.3 Posterior model correlations of shape and size due to remanent magnetization

To provide a deeper perspective on the variation of the model parameters due to remanent magnetization, an example study on two targets (target 4: 155 mm grenade and target 21: A depth charge ordnance, the largest UXO in the study) is showcased, where effort has been put into sampling a broader region of the posterior distribution. This is done by increasing the sampling length and splitting the sampling process up into intervals of different prior assumptions of remanent magnetization (hereby forcing it around in the model space). The Gibbs sampling is set to nearest neighbour interpolation (with low sampling density) to increase the exploration rate. This can result in bad model samples with low likelihood, but these are removed by cutting off samples with an obvious jump in likelihood, ensuring that no bad samples are considered while supporting a higher exploration rate of the model space.

Inversion of the lower single-sensor data will be used since this data set is easier to sample and provides sufficient constraints on the fitting dipole moment. 2-D marginal distributions of chosen model samples are illustrated in Fig. 12 for all three shape-oriented forward models. The model parameters in focus are *kg steel* (i.e. volume), *Mrem*, *Theta* and *Phi*. The aspect ratios are left out for the prism and spheroid models because they are not of much relevance to compare.

In terms of depth estimation, the estimate is generally so well-resolved that the values are close to identical for all three forward models (within centimetres of range). This is due to the uncorrelated noise model being used, when utilizing the correlated noise models the precision generally decreases in the inversion estimates. For instance, considering targets 21–24, When computing the average depth estimate using the several noise models introduced, the depth estimates all lie within ± 0.4 m of the expected location of the target centre. Positioning of sources from inversion is discussed in Kolster *et al.* (2022) where similar depth estimates are obtained when utilizing different inputs of data input from the triple sensor setup.

Inspection of Fig. 12 shows a general high variation in weight estimates, with a high correlation between the modelled remanent

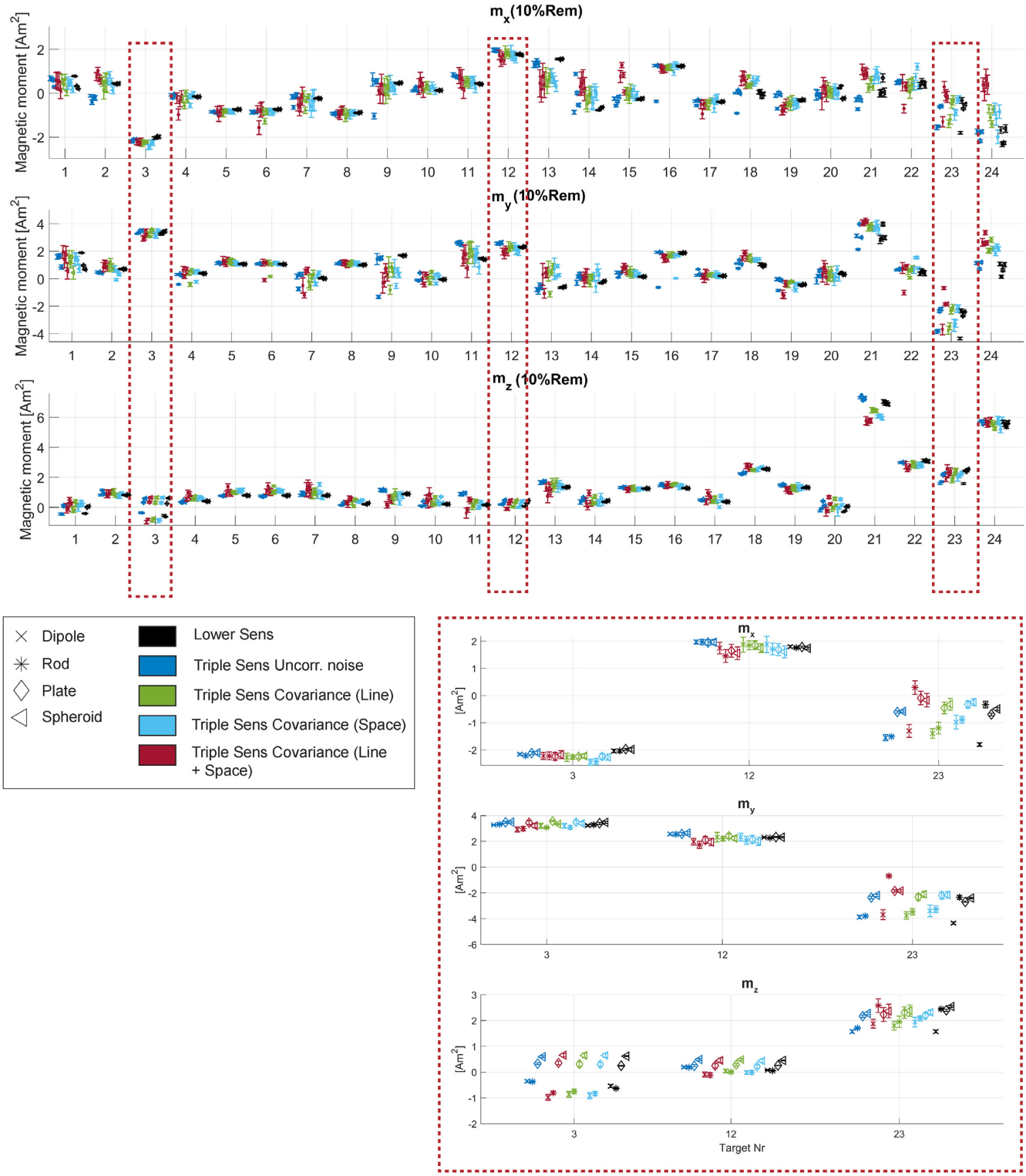

Figure 8. Mean estimated moments derived with remanence 10 per cent, for all three classes (rod, plate, spheroid) together with the simple dipole model. The moments are estimated by taking a mean of the last 5 posterior samples (and error bars of the standard deviation of the last 10 samples). The only case where some discrimination is seen is for targets 3, 12 and 23. These are highlighted in a focused figure bottom right.

magnetization strength and kg steel. For target 21, a clear trend between the kg steel and *Mrem* is apparent in the model parameters of the spheroid inversion. The amount of steel generally decreases when the remanent magnetization is increased. If only the solutions with $Mrem < 0.4$ are taken into account, then the estimated weight of steel would be approximately between 380 and 700 kg. Considering that target 21 weighs 48 kg, an estimate of 380 and 700 kg seems far off and indicates that the relative remanent magnetization is much higher in the source than the prior allows. As is evident from Fig. 12, it can be seen see that the estimated volume of steel for target 21 is

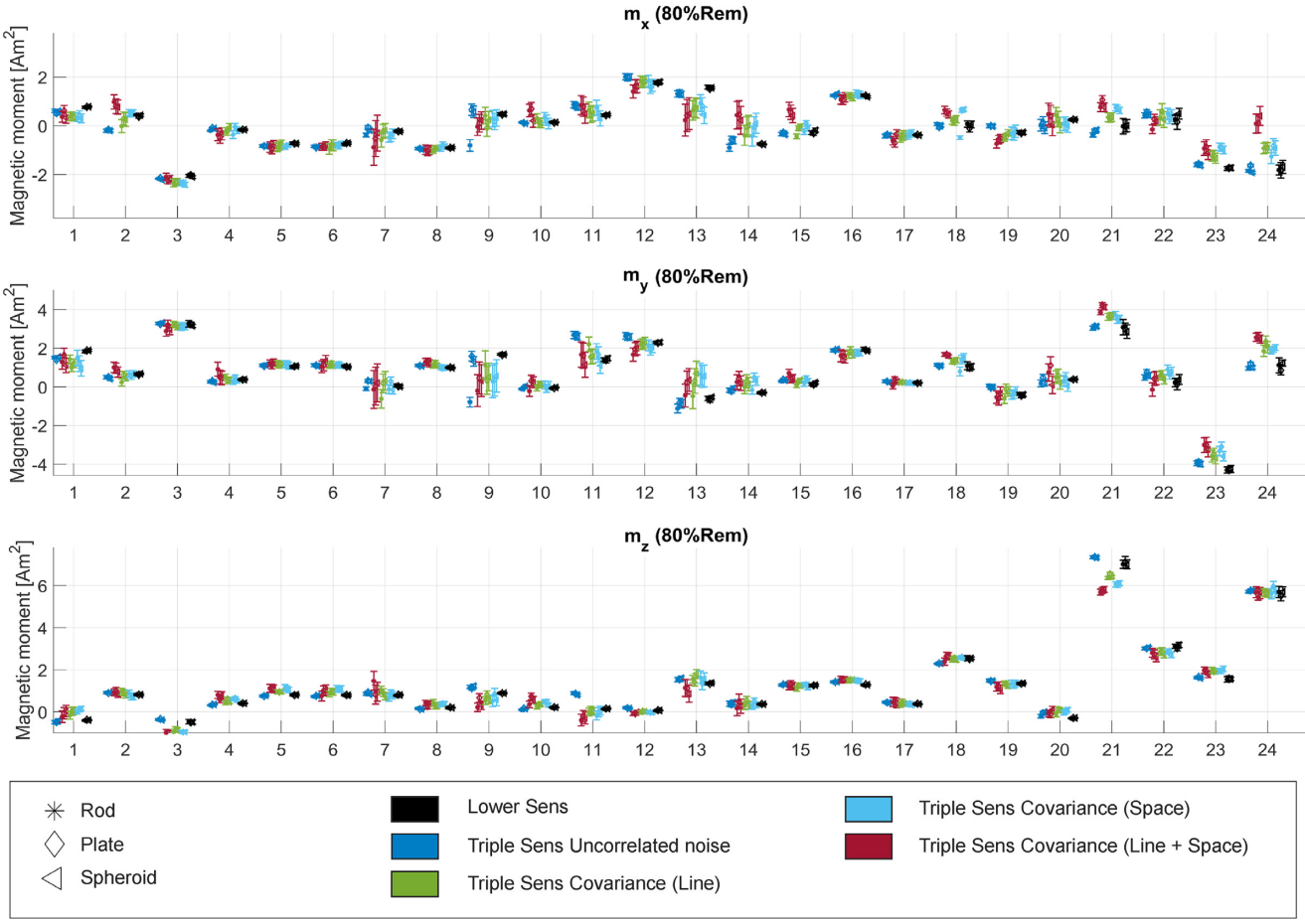

Figure 9. Mean estimated moments for all shape inversions with remanence up to 80 per cent. (almost) all inversions here have converged to equal log$L$-values (there is no discrimination case in any of these). The plot gives an idea of the variance in the estimated moments for the different noise models and forwards when inversion of the anomaly is carried out with the noise models.

much lower (many samples around 60–100 kg) when the remanence is above 50 per cent. In this region the estimated kg steel is close to the true value, indicating that the relative remanence is significant (+50 per cent) in this particular object. Some modelling errors may influence the estimated model parameters. For example, target 21 is not spherical but more cylindrical and has several metal hinges on each of the ends. This could influence the magnetic signature and thus the predicted aspect ratio, which is estimated to be around 6 when the kg steel is around the expected range of 50 kg (the aspect ratio of target 21 is closer to aspect ratio = 2). However, this may only have a minor influence on the model prediction. Remanent magnetization in the source is still believed to have a more significant influence on the prediction of shape.

For target 4, the posterior samples in Fig. 12 indicate a lower relative remanence in the source. This item weighs about 25 kg, which is mostly seen in the posterior samples when the remanence is low (albeit some low volume samples are also with high remanence). The maximum estimated kg steel for the 155 mm is approximately 85 kg when the remanent magnetization is around 50 per cent.

In Fig. 13, the posterior samples (shown in Fig. 12) have been used to generate the estimated magnetic dipole moments. For both target 21 and 4, it is evident that despite the high variation in the posterior samples of weight and remanent magnetization, the resulting dipole moment is similar. As an example, the spheroid samples for target 21 model kg-steel values between 50 and 750 kg, illustrating the high uncertainty in shape and size due to the remanent magnetization.

Examples of induced and remanent components from the spheroid inversion are shown in Fig. 14. These are the same spheroid samples as shown in Figs 12 and 13 for targets 4 and 21, but the sampled components of induced and remanent magnetization are here shown. Three figures are made for each target, with the left-most plot showing the induced moment, remanent moment and the combined moment for all samples. In the second plot only cases with low volume (lowest 5–10 per cent of posterior) appear and in the third only samples with high volume (highest 5–10 per cent of posterior) are shown. It is evident from both target examples, that when the model has high volume (high induced moment), then the remanent magnetization is, to some degree, facing opposite of the induced or ambient field. When the volume is low (i.e. middlemost plot), then the direction of remanent is fairly constrained (For both targets, these results are within a reasonable range of the actual weight suggesting that the actual remanent magnetization could be represented in these samples).

4 DISCUSSION

It is evident from this study, that remanent magnetization in UXO/non-UXO sources is indeed something that has to be assessed when doing any inference of source shape solely from the

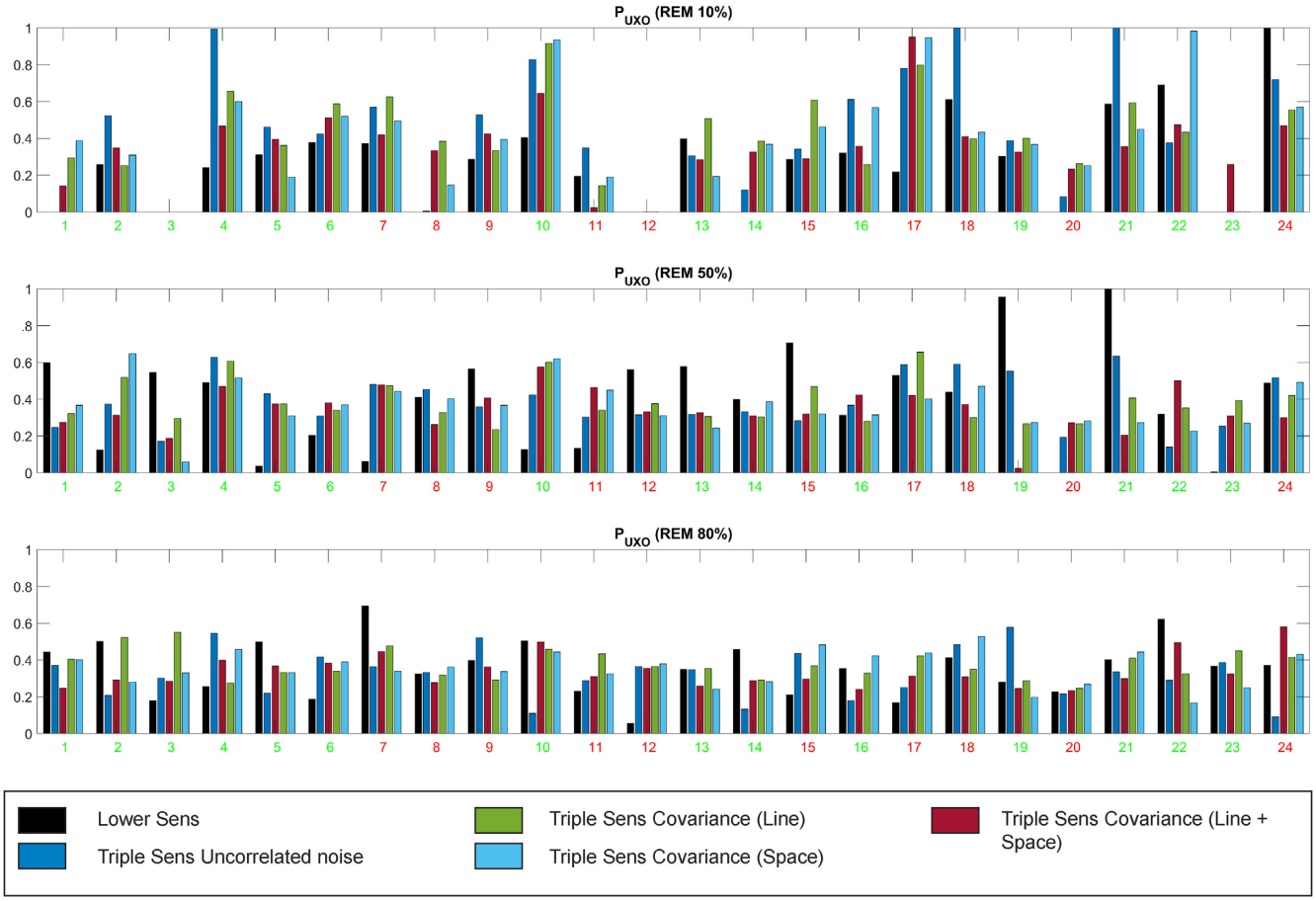

Figure 10. Overview of all shape inversions, illustrating the estimated class probability of the spheroid (P_{UXO}) for the different inversion setups. The P_{UXO} is calculated from the relative probabilities of the spheroidal forward model. The target numbers (x-axis) are colour coded to indicate if a target is an UXO (green) or non-UXO (red).

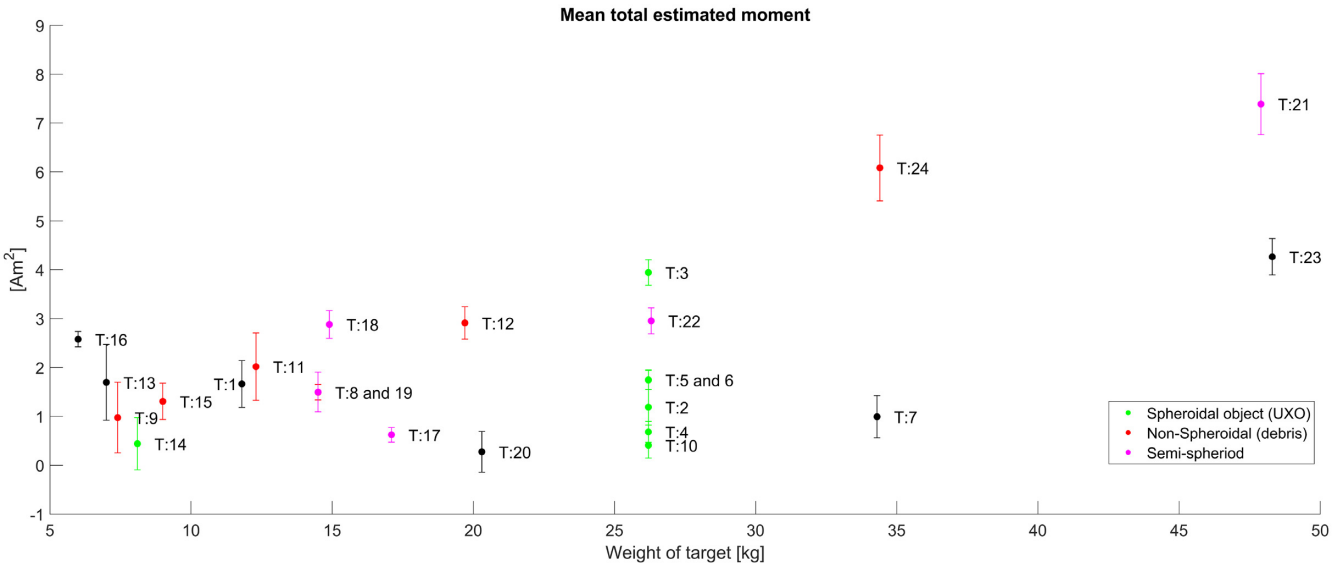

Figure 11. Overview plot of estimated dipole moment for each target, sorted by weight. The error bars are estimated by averaging over the different inversion estimates. It is computed by taking an average of the individual STDs of the last eight posterior samples of the different inversion setups, together with the standard deviation between the mean estimates of the five inversion setups. The targets are grouped into three colour groups: Green: objects with an 'obvious' spheroidal shape, Red: non-UXO objects with no spheroidal resemblance. Purple: Items with semi-spheroidal shapes (primarily cylinders).

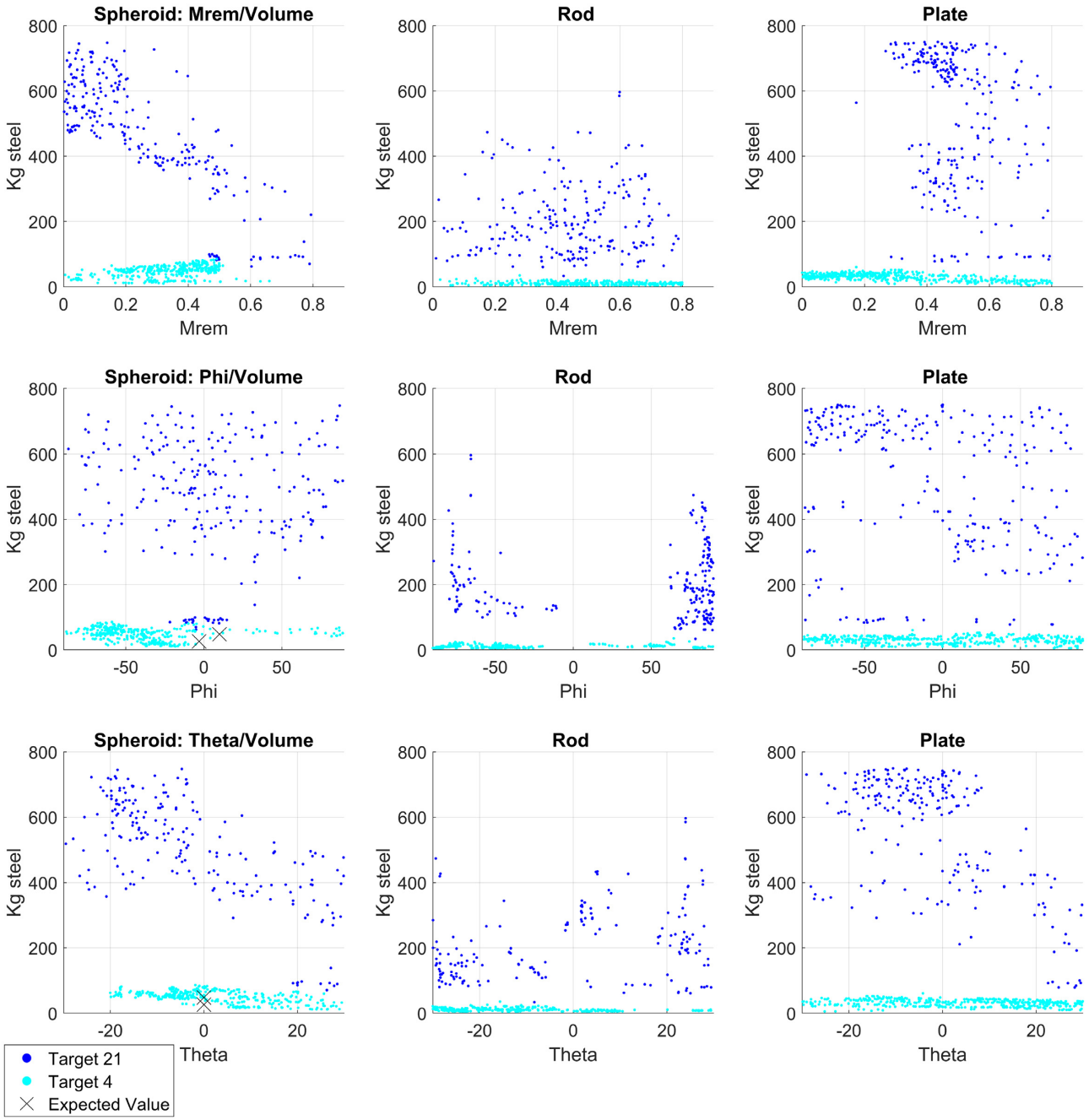

Figure 12. Analysis of model parameter variations due to remanent magnetization and orientation of the targets. The analysis is made for the three forward models: Prolate-(Spheroid), Rod-(Prism), Plate-(Prism) for two different anomalies (Target 4: Light blue and Target 21: Dark blue). 2-D marginal posterior distributions are shown for the model parameters; Volume, Phi (Objects long axis angle with respect to north, *Theta* (dip of the object with respect to a flat surface).

magnetic anomaly. Remanent magnetization may cause significant changes to the amplitude and direction of the magnetic moment of the source, which complicates any discrimination significantly. It is evident from the inversions, having 10 per cent remanent magnetization strength allowed in the prior, that some discriminatory capabilities are possible (e.g. target 12). However, a low remanent magnetization also introduces scenarios where an item might be falsely classified as a non-UXO (e.g. target 3). Therefore, it must be concluded that discrimination seems difficult unless additional constraints can be put on the remanent magnetization of the source. Similarly, the non-uniqueness of the problem could be reduced if more information was obtained about the source such as its aspect ratio and orientation. For this study, the prior constraints on the orientation of the targets were low in order to quantify the classification. The Phi angle (angle between the object's long axis and geomagnetic north) was unconstrained while the *Theta* angle (long axis dip of the object relative to the surface) was limited between –35° to 35°. This is quite high, considering that the targets were positioned on a flat beach area (i.e. all targets have been positioned flat on the surface such that *Theta* < 5). It is most likely that the discrimination procedure would perform better if the *Theta* angle was reduced in the prior, such that objects were assumed to lie flat

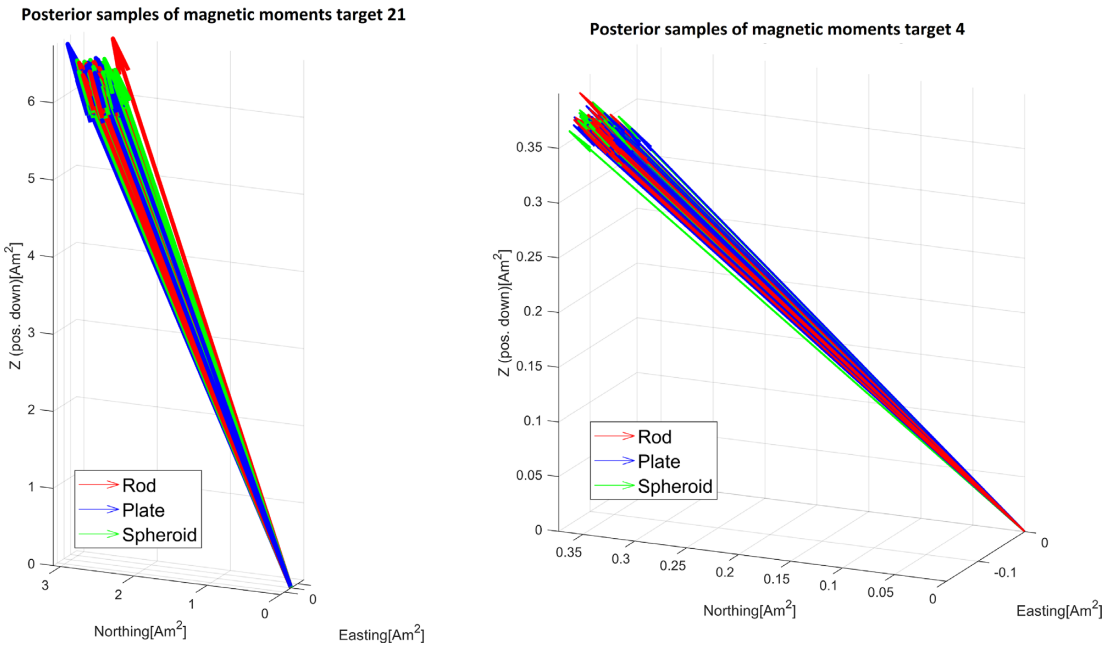

Figure 13. Plot of magnetic vector moments from the samples shown in Fig. 12. The moments are derived using the three different shapes (spheroid, rod, plate) inversions and colour coded according to the legend. Left-hand plot: posterior samples from inversion of target 21. Right-hand plot: posterior samples from inversion of target 4. All samples are produced from inversion using the uncorrelated noise model.

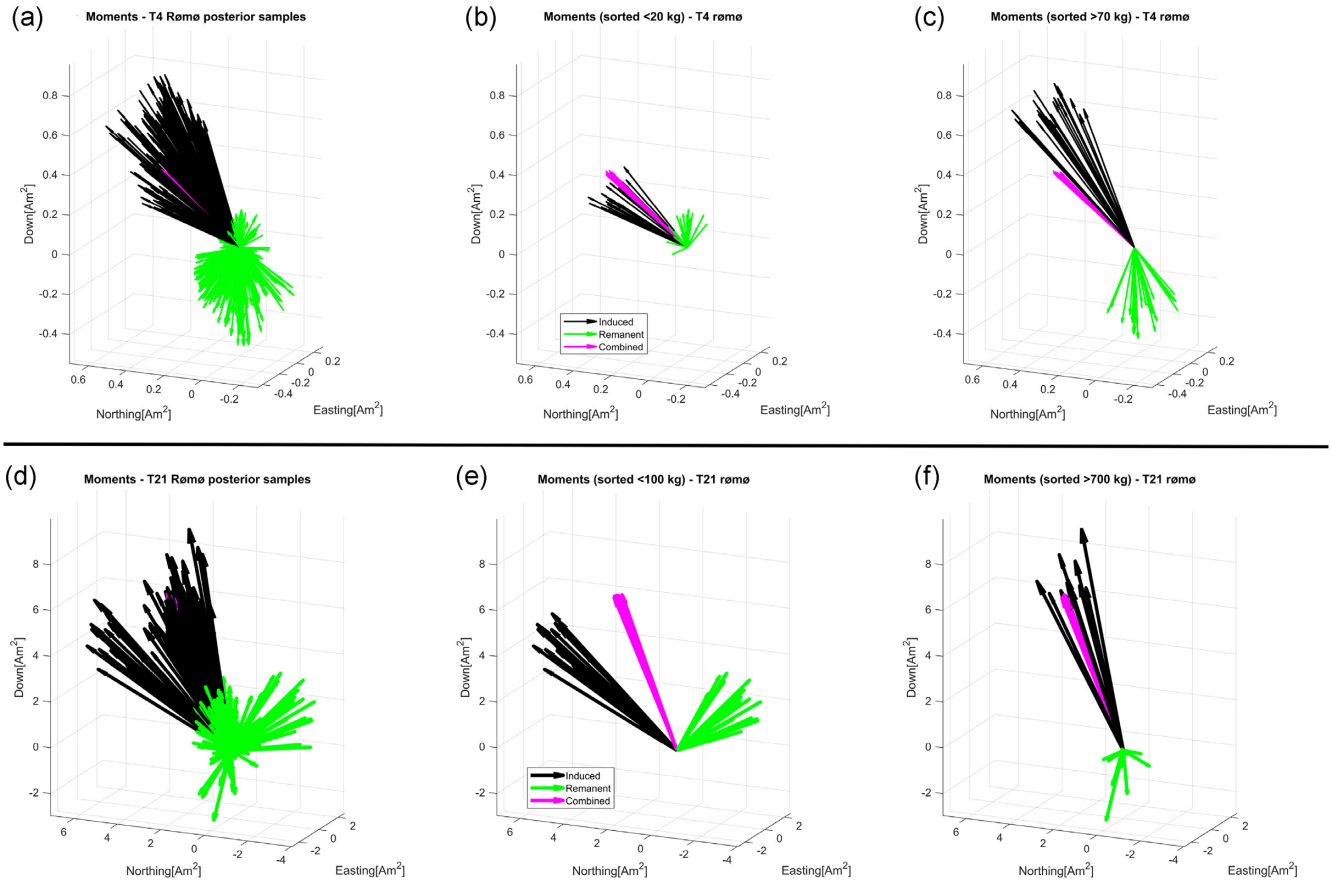

Figure 14. Vector moment plots of the estimated magnetic moments split up in induced and remanent contributions. The moments are generated using the spheroid prior (same results as shown in 2-D posterior of Fig. 12. Top row (Target 4), Bottom row (Target 21); (a and d): Induced and remanent components for all samples used. (b and e): Induced and remanent components for low volume samples only. (c and f): Induced and remanent components for high volume samples only.

on the surface. However, in real-case scenarios, it is hard to exclude the possibility of buried objects where the object might have a significant dip angle. Any information that could be obtained on the orientation or shape of an object could improve the classification significantly. However, magnetics is often the primary remote tool for UXO detection and more accurate estimates of the orientation or shape can first be obtained using local inspection or sensing techniques.

Any constraints made on the remanent magnetization will generally provide an improvement in the resolution of estimated shape and size parameters. One idea could be to try and limit the variation due to remanent magnetization in the forward model by defining the remanent contribution as a fixed range of values that are dependent on expected remanence per volume steel instead of relative strength with the induced moment. A range on remanence per cubic meter of steel could potentially be interesting to implement in the modelling process. This would reduce the number of correlations due to variations in the relative remanence, size and orientation of the source, by making the sampled remanent magnetization independent of the object shape and orientation. An alternative way to limit the effects of remanent magnetization could be to constrain the direction of the remanent moment if, for instance, the remanent magnetization were subject to temporal changes (viscous remanent magnetization) aligning it with the ambient field for a stationary source. However, this would require unlikely assumptions in the prior model. 2-D marginal analysis of the kg steel and the remanent strength (*Mrem* in per cent) for target 21 in Fig. 12 suggests, that a remanence at least above 50 per cent is necessary to estimate a somewhat correct amount of steel (i.e. 50 kg). This limit is rather high and complicates any certain characterization of source shape/size.

A number of different noise models were used in the study to account for uncertainties in the model predictions, where three covariance models were used to simulate correlated errors and noise in the data. As magnetic survey data often contain highly correlated noise from other sources and likely correlated sensor errors, it seems essential to have a more realistic description than a simple assumption of uncorrelated noise. We see some improvements in the inversions when using the three covariance models (in many cases the sampling is easier, and likelihood values converging to $\log L = -N/2$ suggesting a more consistent description of the system), yet the noise models used are probably far from realistic and do only account for some errors (or maybe the noise models actually imply errors). Inversion using correlated noise models appears to be quite efficient without biasing the model prediction, as long as the covariance models are appropriately scaled and much lower than any uncorrelated noise. A much higher likelihood is obtained with the covariance models (e.g. $\log L$ closer to $-N/2$), suggesting that we are describing the noise better than the cases with uncorrelated noise models. Caution, however, must be taken since a high likelihood could be obtained by creating a covariance model that describes the anomaly signal patterns as noise (this was experienced in earlier cases, where a high covariance model obtains a different magnetic moment that clearly does not fit the anomaly signal properly).

The line covariance model seems as a simple and efficient way to account for some of the errors that are encountered while optimizing the sampling, without causing any error biases to the spatial features of the anomaly. The increased efficiency is most likely highest when using all triple sensors for the inversion due to the high correlation between the three sensors along each flyover. There were no tests with correlated noise models when using the single sensor data set. However, sampling difficulties seem to occur for some targets, which may have been mitigated by using one of the three covariance models, especially when considering that the lower sensor inversion is carried out with a high noise assumed (SNR of 3).

The inversion with a dipole-moment model has previously been made on the triple-sensor data set (Kolster *et al.* 2022), where the optimal data configuration (single sensor, multiple sensors, horizontal/vertical gradients between sensors) was investigated by inversion. This was carried out using an uncorrelated noise model for all configurations with a fixed SNR, but it does have certain similarities to this study on the handling of noise. Taking the difference between the sensors is principally a matter of increasing the signal-to-noise ratio, making it more applicable to use a simple uncorrelated noise model (assuming other longer wavelength signals are diminished in the gradient differences). Taking the gradient differences can be a strong method to highlight the shorter wavelength signals that originate from near-surface sources. However, the gradient may also cause significant data biases due to the enhancement of errors when one or more sensor differences are used. This could be avoided by applying a correlated noise model on the triple sensor data without taking any gradient differences, which has proven useful as long as a somewhat realistic covariance model is applied. Both methods are applicable with their pros and cons and could be used in synergy to increase the robustness. A combination of the two is also possible but would require a rather complex covariance model if it were to account for data errors due to sensor gradient differences.

Only a few of the estimated magnetic moments have a direction pointing away from the direction of the geomagnetic field. This suggests, that there are few targets with a remanent magnetization facing opposite/perpendicular from the geomagnetic field (assuming there are no cases where the remanence is exactly opposite to the induced moment). Only target 3 and potentially target 23 show a significant deviation in direction from the expected induced moment. One could expect that more targets had a deviation in direction of the magnetic moment due to the presence of remanence, and the fact that the targets were placed out randomly in the survey area on the same day as the survey (i.e. any viscous remanence is negligible and most likely not parallel to the geomagnetic field).

The covariance models have a fixed variance for all targets, so targets with a small anomaly amplitude will have a higher model uncertainty on the estimated moments, while the larger anomalies are expected to have a higher model resolution. It is apparent, however, that the estimated moments for targets 21 and 24 have a high variation between the estimates from the inversion setups, especially when considering the high magnetic moments. These two cases appear to be caused by a residual offset between the data and model prediction of a single survey line just above the target (examples shown in Section 3.2 for target 21). This can be due to several reasons such as higher-order moments due to the line being closer to the target, or due to positional uncertainties in the height of the survey line. In either case, using different noise models gives a qualified perspective of the robustness in the estimated moments and may highlight any inconsistencies between data and noise in the modelling.

5 CONCLUSIONS

Magnetic anomalies of 24 UXO-related objects have been investigated in an attempt to classify and discriminate between UXO and non-UXO targets. Inference of the magnetic anomalies was carried out in a probabilistic inversion approach, where shape and size were inferred by simulating magnetic signatures from prolate spheroids

and rectangular prisms. The inversions were carried out for different assumptions of remanent strength in the prior. It was apparent that discrimination only seemed possible for the lowest assumption of remanence (10 per cent of the induced moment). At this range, two objects were correctly classified while the third, a 155 mm grenade, was wrongly classified as a prism rod, suggesting that a remanent magnetization strength of 10 per cent is insufficient to represent the actual source characteristics. When assuming a higher remanent magnetization strength, no discrimination among the targets was possible. The inversion results suggest that some targets have a strong remanent magnetization (+50 per cent). This indicates, that it is hard to predict any certain discrimination between the 24 targets using magnetics. The discrimination success may have been higher if the shapes of the non-UXO objects were deviant from the UXO shapes, for instance, if the aspect ratios of non-UXO were much higher (provided that any presence of UXO with similar aspect ratios can be excluded). However, the presence of remanent magnetization has a large influence on the discrimination success. Any prior information obtained on expected remanent magnetization strength, as well as the direction of the remanent magnetization (assumptions on direction of remanence might be relevant for UXO that have been in an idle position for many years), could prove to be very valuable in future discrimination projects of UXO/non-UXO when using magnetics. In the study, several covariance models were utilized for handling of correlated noise, illustrating one method to address noise in an inversion of magnetic survey data. The covariance models can be used instead of, or in combination with, a simple uncorrelated noise model to obtain a more robust uncertainty quantification. Utilizing covariance models to simulate correlated noise may also improve sampling efficiency and exploration rate in the inversion process.

DATA AVAILABILITY

Raw data were generated at DTU Space, CMAGTRES group. Derived data supporting the findings of this study are available from the corresponding author (M.D. Wigh) on request.

REFERENCES

Altshuler, T.W., 1996. Shape and orientation effects on magnetic signature prediction for unexploded ordnance, in *Proceedings of the UXO forum 1996*. Williamsburg, VA, pp. 282–291.

Billings, S.D., 2004. Discrimination and classification of buried unexploded ordnance using magnetometry, *IEEE Trans. Geosci. Remote Sens.,* **42**(6), 1241–1251.

Billings, S.D., 2006. Magnetic models of unexploded ordnance, *IEEE Trans. Geosci. Remote sens.,* **44**(8), 2115–2124.

Billings, S.D., 2006. Experiences with unexploded ordnance discrimination using magnetometry at a live-site in Montana, *J. appl. Geophys.,* **61,** 194–205.

Billings, S.D., 2009. Field measurements of induced and remanent moments of unexploded ordnance and shrapnel, *IEEE Trans. Geosci. Remote Sens.,* **47**(3).

Butler, D.K., Cespedes, E.R., Cox, C.B. & Wolfe, P.J., 1998. Multisensor methods for buried unexploded ordnance detection, discrimination and identification, Tech. Rep. SERDP-98-10, U.S. Army Engineer Waterways Experiment Station, Vicksburg, MS.

Cunningham, M., Samson, C. & Laliberté, J., 2021. Inversion of magnetic data acquired with a rotary-wing unmanned aircraft system for gold exploration, *Pure appl. Geophys.,* **178,** 501–516.

Døssing, A., Lima Simões da Silva, E., Martelet, G., Rasmussen, T.M., Gloaguen, E., Petersen, J.T. & Linde, J., 2021. A high-speed, light-weight scalar magnetometer bird for km scale UAV magnetic surveying: on sensor choice, bird design, and quality of output data, *Remote Sens.,* **13**(4), 1–24.

Geman, S. & Geman, D., 1984. Stochastic relaxation, Gibbs distributions, and the Bayesian restoration of images, *IEEE Trans. Pattern Anal. Mach. Intell.,* (6), 721–741.

Hansen, T.M., Moesgaard, K. & Cordua, K.S., 2008. Using geostatistics to describe complex a priori information for inverse problems, in *GEOSTATS 2008: Proceedings of the Eighth International Geostatistics Congress,* pp. 329–338.

Hansen, T.M., Cordua, K.S., Looms, M.C. & Moesgaard, K., 2013a. SIPPI: a Matlab toolbox for sampling the solution to inverse problems with complex prior information: Part 1, methodology, *Comput. Geosci.,* **52**(3), 470–480.

Hansen, T.M., Cordua, K.S., Looms, M.C. & Moesgaard, K., 2013b. SIPPI: a Matlab toolbox for sampling the solution to inverse problems with complex prior information: Part 2. Application to crosshole GPR tomography, *Comput. Geosci.,* **52**(3), 481–492.

Hansen, T.M., Cordua, K.S., Jakobsen, B. & Moesgaard, K., 2014. Accounting for imperfect forward modeling in geophysical inverse problems—exemplified for crosshole tomography, *Geophysics,* **79**(3), H1–H21.

Kolster, M.E. & Døssing, A., 2021a. Simultaneous line shift and source parameter inversion applied to a scalar magnetic survey for small unexploded ordnance, *Near Surf. Geophys.,* **19**(6), 629–641.

Kolster, M.E. & Døssing, A., 2021b. Scalar magnetic difference inversion applied to UAV-based UXO detection, *J. geophys. Int.,* **224**(1), 468–486.

Kolster, M.E., Wigh, M.D., Lima Simões da Silva, E., Bjerg Vilhelmsen, T. & Døssing, A., 2022. High-speed magnetic surveying for unexploded ordnance using UAV systems, *Remote Sens.,* **14**(5).

Mosegaard, K. & Tarantola, A., 1995. Monte Carlo sampling of solutions to inverse problems, *J. geophys. Res.,* **100**(B7), 12 431–12 447.

Mosegaard, K. & Tarantola, A., 2002. Probabilistic approach to inverse problems, *Int. Geophys.,* **81,** 237–65.

Mosegaard, K. & Sambrigde, M., 2002. Monte Carlo methods in geophysical inverse problems, *Rev. Geophys.,* **40**(3), 1–3.

Tarantola, A., 2005. *Inverse Problem Theory and Methods for Model Parameter Estimation,* SIAM.

Walter, C., Braun, A. & Fotopoulos, G., 2020. High-resolution unmanned aerial vehicle aeromagnetic surveys for mineral exploration targets, *Geophys. Prospect.,* **68**(1), 334–349.

Wigh, M.D., Hansen, T.M. & Døssing, A., 2020. Inference of unexploded ordnance (UXO) by probabilistic inversion of magnetic data, *J. geophys. Int.,* **220,** 37–58.

Wigh, M.D., Hansen, T.M. & Døssing, A., 2021. Synthetic case study: discrimination of unexploded ordnance (UXO) and non-UXO sources with varying remanent magnetization strength using magnetic data, *J. geophys. Int.,* **228**(2), 773–791.